Optimization Approaches for RMS Current Reduction of Triple Active Bridge Converters

Ahmed A. Ibrahim, Andrea Zilio, Davide Biadene, Tommaso Caldognetto, Paolo Mattavelli
Dept. of Management and Engineering (DTG)
University of Padova, Vicenza, Italy
Email: ahmedadelaly.ibrahim@phd.unipd.it, andrea.zilio.5@phd.unipd.it, davide.biadene@unipd.it, tommaso.caldognetto@unipd.it, paolo.mattavelli@unipd.it

***Abstract*—Isolated multi-port converters can interconnect different loads and energy sources at their ports, while utilizing a limited number of switching devices and magnetic components, which offers potential advantages in terms of power density. However, being the multiple ports coupled among each other, the number of modulation variables and operating modes increases, which poses challenging optimization issues. This paper exploits three different optimization approaches used to optimize the performance of a triple active bridge converter (TAB) by minimizing the ports total true rms current. The three approaches shown herein are based on an offline gradient descent search, online multidimensional ripple correlation search, and artificial neural network. All the approaches are validated through simulation and experimental results considering a TAB converter prototype rated 5 kW.**

***Index Terms*—Multi-port converter, triple active bridge (TAB), rms current optimization.**

I. Introduction

Isolated multi-port converters (IMPC) allow hosting different sources and loads with different voltage and power levels at their ports [1]–[4], while ensuring galvanic isolation between these ports and offering potential advantages in terms of power density. These features make such converters suitable in different applications such as electric vehicles, electric aircraft, and micro and nano grids [5]–[8].

The triple active bridge converter (TAB) is an IMPC with three ports [9], [10], as shown in Fig. 1(a). The TAB consists of three full bridges connected to a three-terminal high-frequency transformer. Power flow control among the ports is performed by controlling the phase-shifts (i.e., ϕ_2, ϕ_3) among the ports voltages (i.e., v_1, v_2, v_3). The phase-shift magnitude allows to regulate the magnitude of the power flow, with maximum phase shift at $\pi/2$, while the phase-shift sign controls the power flow direction, with positive power flow from the leading port to the lagging port. This basic modulation method is known as phase-shift modulation (PSM) [11], and it is illustrated in Fig. 1(b). PSM modulation shown to provide simplicity and good conversion efficiency while operating at moderate-to-high power levels with matching voltages at port terminals (i.e., $V_1 : V_2 : V_3 = n_1 : n_2 : n_3$). At these conditions, PSM achieves low conduction loss and zero voltage switching (ZVS). However, at low power operation and voltage mismatch at the ports terminal, PSM brings to relatively high conduction loss and loss of ZVS, with overall performance substantially far from optimal [11].

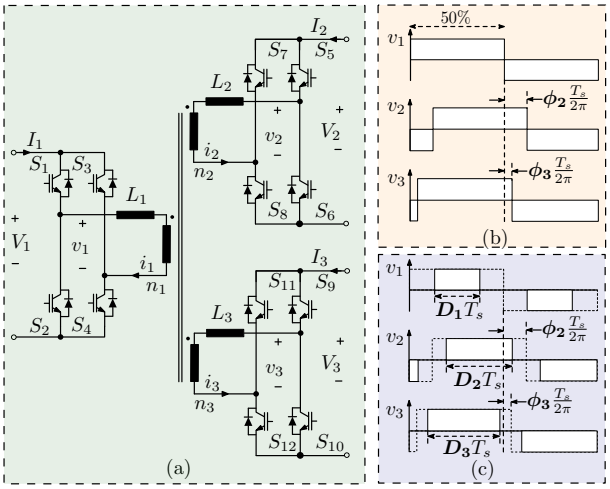

Fig. 1. (a) Triple active bridge converter; (b) phase-shift modulation; (c) penta phase-shift modulation. Modulation variable $\phi_2, \phi_3, D_1, D_2, D_3$ highlighted.

Penta phase-shift has been proposed in [11], utilizing the voltages duty cycles (i.e., D_1, D_2, D_3) besides the phase-shifts, as shown in Fig. 1(c). To exploit the duty cycles, increases the modulation variables from two to five, with total possible voltage switching patterns 6! = 720. This complicates the optimization problem of finding the optimum pattern for minimum converter loss using normal analysis tools. The literature reports several relevant optimization methods [11]–[14]. In [11], The optimization of the total converter loss was limited to the fundamental component, ignoring the harmonics. The assumption in [11] is valid for medium to high powers, while at low power levels, the effect of harmonics increases. In [12]–[14], an analysis of the converter in the frequency domain has been investigated. However, the frequency domain analysis depends on many assumptions, which may limit model generality.

This paper describes and compares three different optimization approaches capable of reducing the TAB converter conduction loss by means of minimizing the total true rms current. The first approach is based on a time domain analysis of a set of selected favorable switching patterns [15]. The second optimization technique is a model-free technique based on the ripple correlation search, a form of extremum seeking

TABLE I
SIMULATION PARAMETERS OF BF,VALUES ARE REFERRED TO V_1

Parameters		Value
Nominal power at each port P_{rated}	kW	5.5
Switching frequency $f_S = 1/T_S$	kHz	40
Port-1 rated voltage V_1	V	300
Port-2, Port-3 rated voltage V_2, V_3	V	400
Transf. leakage inductance $L_1 = L_2 = L_3$	µH	25
Transf. turns ratio $n_1 : n_2 : n_3$		30:40:40

algorithm [16]. The last approach is based on an artificial intelligence method, in which an artificial neural network is trained offline to make a TAB converter operate with minimum circulating rms currents [17].

II. Optimization Approaches for Minimum TAB rms Current

This section reports a study of three different optimization approaches. The approaches aim to find the minimum total true rms current defined as:

$$i^{rms} = \sqrt{\sum_{p=1}^{3} r_p \left(i_p^{rms}\right)^2} = f(\phi_2, \phi_3, D_1, D_2, D_3) \qquad (1)$$

where weights r_p, $p = 1, \ldots, 3$, are the equivalent path resistances of the respective p-th port. Notably, the total true rms current depends on five modulation parameters, which are two phase shifts (i.e., ϕ_2, ϕ_3) and three duty cycles (i.e., D_1, D_2, D_3). The three optimization methods optimize the total true rms current in (1) by searching for the optimum duty cycles while the phase shifts are adjusted by means of a couple of PI regulators in order to regulate the converter output voltages (i.e., V_2, V_3). The input voltage to the converter (V_1) is imposed by an external dc supply.

The principal concepts and simulation results for each technique are discussed in the following, while experimental validations are reported in Sect. III.

A. Offline Gradient Descent Optimization

This approach is performed in three steps:

1) Search for a favorable switching pattern achieving minimum true rms current.
2) Constructing a mathematical model of the favorable pattern.
3) Optimizing the mathematical model by gradient descent algorithm (GDA).

The first step is a systematic brute-force (BF) search of the optimal points on the duty cycles D_1, D_2, and D_3. The search is performed offline on Matlab/Simulink with parameters listed in Table. I. Fig. 2 shows simulation results of the BF search at one set point defined with $P_2 = 400$ W, $P_3 = 100$ W, $V_1 = 300$ V, $V_2 = 320$ V, and $V_3 = 280$ V. In Fig. 2(a) the x-axis describes different combinations of duty cycles, each segment identified by the labels on top of the figure has a constant duty cycle D_1, while D_2 and D_3 vary with a fixed step in their domain. Fig. 2(b) shows a zoom-in view of the third segment of Fig. 2(a), where D_1 is fixed at 0.14, where

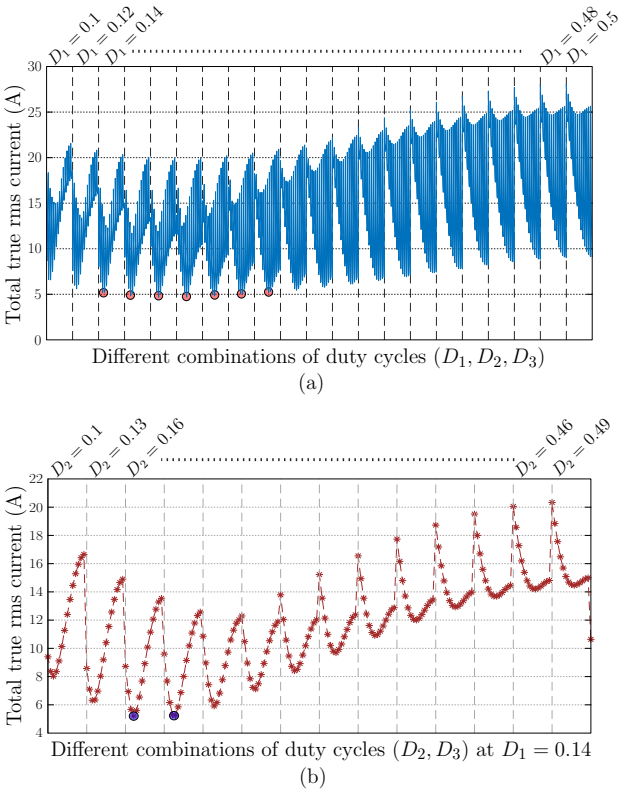

Fig. 2. Simulation results at set point $P_2 = 400$ W, $P_3 = 100$, W, $V_1 = 300$ V, $V_2 = 320$ V, $V_3 = 280$V: (a) total true rms current for different combinations of the three duty cycles; (b) total true rms current at fixed $D_1 = 0.14$ with different combinations of D_2 and D_3.

the x-axis can be interpreted as different combinations of D_2 and D_3, with fixed D_2 inside each segment labeled on top of the figure. Notably, Fig. 2 shows that different combinations of duty cycles, corresponding to different switching patterns, can give similar values of minimum true rms current. In this case, the switching pattern covering the wider range of operating conditions should be used. The found pattern is considered as the favorable pattern for low power level operation, Fig. 3(a) shows the range of the favorable pattern for the same set-point used in Fig. 2 but with variable power at port-2. Fig. 3(b) shows the benefits from using the found pattern rather than phase-shift modulation (PSM), especially at low power level, where a total true rms current reduction of up to 70% is recorded. Besides, at medium-to-high power levels, PSM results to the same true rms current.

By applying this search technique to the whole power and voltage range of operation of the converter results in the six switching patterns in Fig. 4, these present the most favorable loss performance with different voltage levels.

A second step is to derive a closed-form analytical representation for the true rms current, as:

$$i^{rms} = f(D_1,\, D_2,\, D_3,\, P_2,\, P_3,\, \Sigma_{par}) \qquad (2)$$

Where, Σ_{par} is the converter parameters. This approach is now viable since the number of switching pattern under study are limited by the procedure described above to only six in Fig. 4

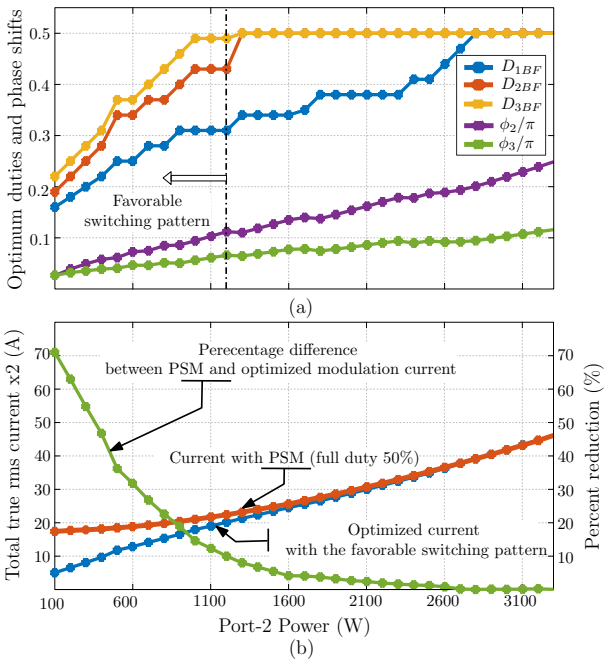

Fig. 3. Simulation results of BF search at the same set point of Fig. 2 with variable P_2: (a) variation of the optimum duty cycles; (b) illustration of the improvements made by the found favorable pattern over PSM.

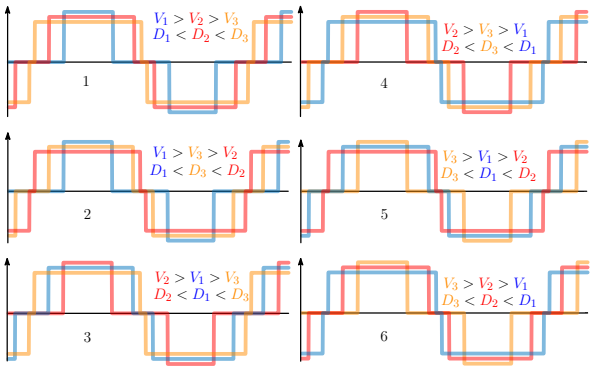

Fig. 4. Six switching patterns for low power level rms current optimization (favorable switching pattern).

– notably, the total number of switching patterns for the TAB amounts to 6! = 720.

After obtaining the total true rms current in closed-form, a search for the modulation parameters to achieve minimum total rms current, which would bring to minimum conduction loss, can be run on the deduced formula. Then, a gradient descent search algorithm is implemented, run offline, and used to build a look-up table (LUT) by the found results.

B. Online Multidimensional Ripple Correlation Search

The second approach described herein is run online, and it does not require any modeling of the converter, namely, it is model-free. The technique is based on the ripple correlation control (RCC) [18], which has the same theoretical framework of extremum seeking control (ESC) [16], where a correlation, positive or negative, is found between two variables. One of these variables is the cost function, specifically, the TAB converter rms current (1), while the other variable is a controllable variable, specifically, the modulation variable. By perturbing the controllable variables and observing the effect of such perturbations on the cost function, the controlled variables are driven in the direction of reducing the cost function. This optimization is based on an estimation of correlation factor (ρ_{xy}) among the two variables obtained by means of the scheme displayed in Fig. 5(a).

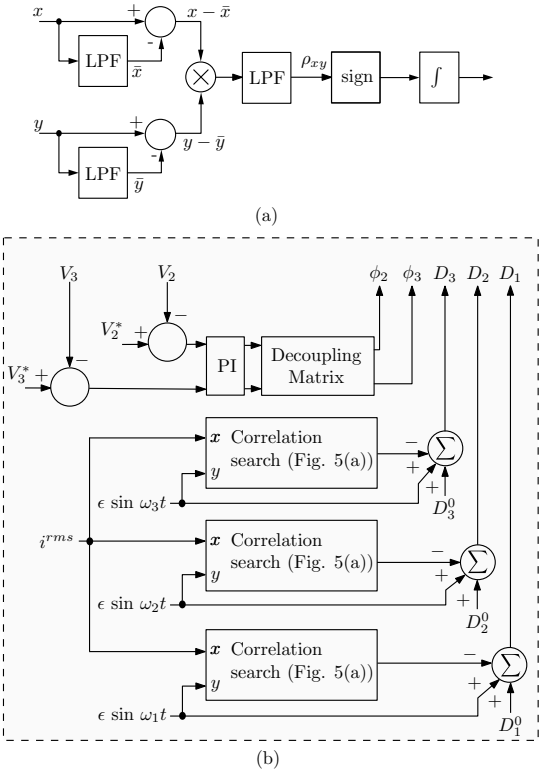

Fig. 5. Ripple correlation search: (a) one dimentional RCC; (b) extended three-dementional RCC (3D-RCC).

Since the control variables herein are three variables (D_1, D_2, D_3), three-dimensional ripple correlation control (3D-RCC) is applied, in which the multidimensional optimization problem is simplified into three separate optimization problems. Orthogonality is obtained between the modulation variables by utilizing three different perturbation frequencies on the modulation variables and observing the effect of each perturbation separately, as shown in Fig. 5(b).

Hardware in the loop (HIL) is utilized in this part to show the efficacy of the 3D-RCC optimization technique. Fig. 6 shows the real-time simulator PLECS RT-Box1 with parameters listed in Table. II. The 3D-RCC search and converter control and modulation are implemented on an Imperix L.t.d. B-Box RCP controller.

The collected results using 3D-RCC are compared to those found by a systematic BF search on the same cost function using HIL validation. On this basis, the results obtained by the BF search are regarded as the true optimum solutions as in Sect. II-A.

Fig. 7 shows the obtained results at $V_1 = 400\,\mathrm{V}, V_2 =$

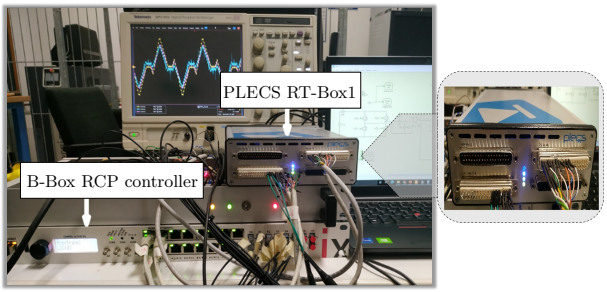

Fig. 6. Hardware-in-the-loop validation setup.

TABLE II
HIL VALIDATION PARAMETERS

Parameters		Value
Nominal power at each port P_{rated}	kW	5
Switching frequency $f_S = 1/T_S$	kHz	5
Rated dc voltages $V_1 = V_2 = V_3$	V	400
Transf. turns ratio $n_1 : n_2 : n_3$		1:1:1
Transf. leakage inductance $L_1 = L_2 = L_3$	µH	350
Sinusoidal disturbance magnitude ϵ		0.01
Sinusoidal disturbance-1 freq. ω_1	rad/s	24π
Sinusoidal disturbance-2 freq. ω_2	rad/s	20π
Sinusoidal disturbance-3 freq. ω_3	rad/s	16π
Simulation integration step	µs	4

320 V, V_3 = 480 V, and P_2 = 350 W, while port-3 power P_3 is changing by a step of 150 W, with total true rms current (1) as optimization objective. Specifically, Fig. 7(a) shows the optimum duty cycles found by the BF search (i.e., $D_{1BF}, D_{2BF}, D_{3BF}$) compared to the 3D-RCC search results (i.e., $D_{1RCC}, D_{2RCC}, D_{3RCC}$). The searching technique gives almost the same duty cycles over the considered P_3 variation. Fig. 7(b) shows the total true rms currents corresponding to the BF search findings and 3D-RCC search findings, with the

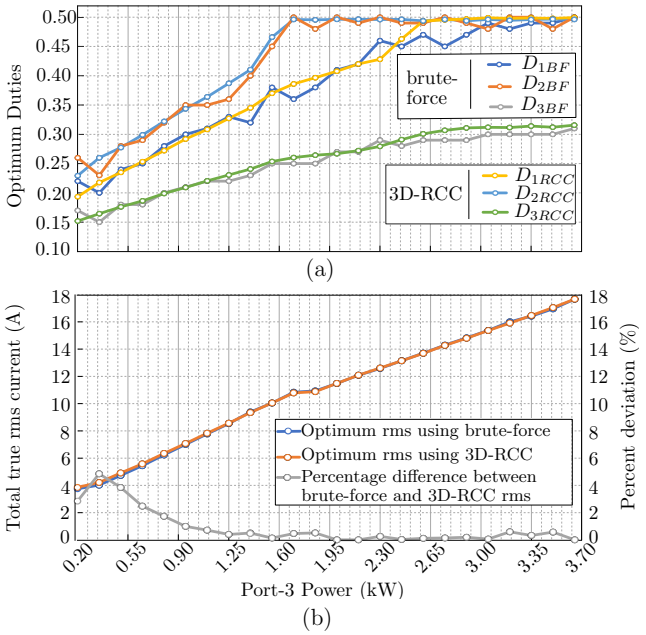

Fig. 7. HIL validation: (a) variation of the optimum duties w.r.t the change in the power level; (b) total true rms current of both BF and 3D-RCC search .

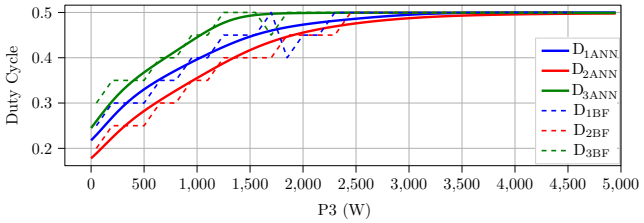

Fig. 8. Fitting of the ANN compared to BF analysis with V_2 = 400V, V_3 = 320V, P_2 = 500, and P_3 variable.

maximum deviation between the two currents of less than 5%.

C. Artificial Neural Network Modulation Based

A modulation based on an artificial neural network (ANN) is then described as third possible approach. This technique involves the training of an ANN to find the minimum total true rms current (1). The complexity of the cost function is overcome by a data-driven approach, exploiting the information collected from a simulation model to compute the optimal TAB modulation parameters for rms current reduction. The training process of the ANN is done in three steps as follows.

1) Simulation model validation and data-set collection.
2) Training of the ANN based on the collected data.
3) Validation of the results on the experimental prototype.

PLECS simulations have been used to generate the data-set used to train the ANN, as done in [19]. The simulation model has been calibrated and validated to match the experimental prototype in Table. IV, considering the actual transformer leakage inductance, switching frequency, deadtime, etc. The matching process includes matching transformer rms current and current and voltage waveforms at several test points. The rms current deviation between the two models is below 10%. Then, a systematic BF search is run on the duty cycles D_1, D_2, D_3, testing about 512 possible combinations of duty cycles for each power and voltage set-point. The search finds duties with minimum total true rms current, and it is repeated for about 15,000 set-points of different ports voltages and powers. The collected data-set represents the BF search findings, with about 15,000 points, which is then used to train the ANN.

An operating points is used to show the performances of the built ANN. The voltages V_2 and V_3 with the power P_2 are kept constant as shown in Fig. 8, the dotted lines are the data obtained from BF analysis and used during the training process while, the continuous lines represent ANN outputs.

Fig. 9 illustrates the flowchart for the three discussed approaches. Table. III shows a comparison between the three approaches features.

III. EXPERIMENTAL RESULTS

A. Laboratory Prototype

The setup in Fig. 10 with a TAB converter prototype with parameters listed in Table. IV and structure in Fig. 11 is considered for experimental validation.

Port-1 of the converter is connected to a fixed dc power supply at rated voltage V_1 = 400 V, while port-2 and port-3

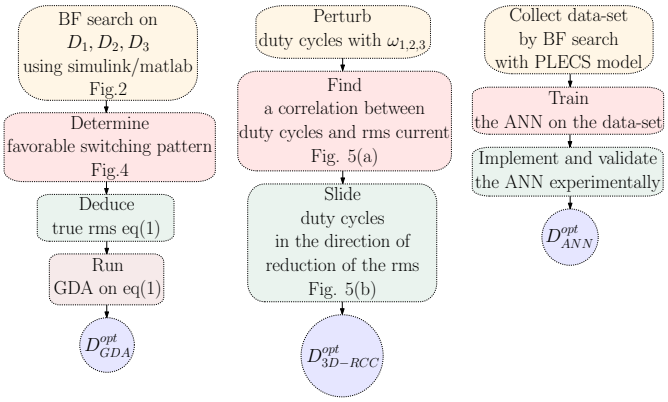

Fig. 9. flowchart of the discussed optimization approaches

TABLE III
COMPARISON BETWEEN THE THREE APPROACHES

optimization	approach	online optimization	core implementation
GDA	closed formula	✗	LUT
3D-RCC	model-free	✓	RCC
ANN	data-driven	✗	ANN-model

are connected to corresponding dc electronic loads. Controls and modulation are implemented on an Imperix L.t.d. B-Box RCP controller driving six Imperix PEB8032-A half-bridges.

To find the five modulation parameters for each set-point, two phase-shifts ϕ_2 and ϕ_3 are adjusted by employing two separate linear regulators followed by a decoupling matrix, as in [11]. Duty cycles D_1, D_2, and D_3 are generated from the corresponding optimization approach.

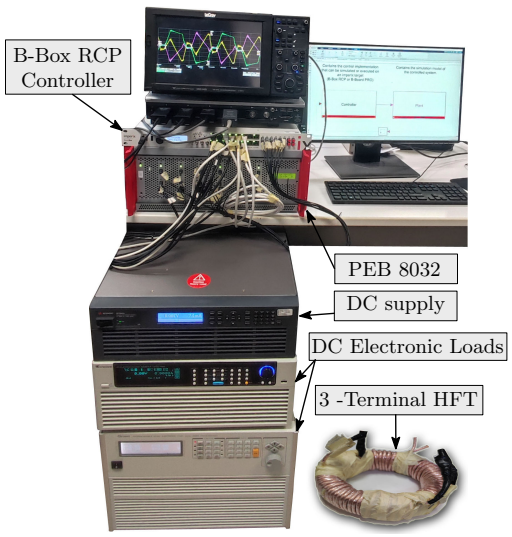

Fig. 10. Laboratory prototype of TAB.

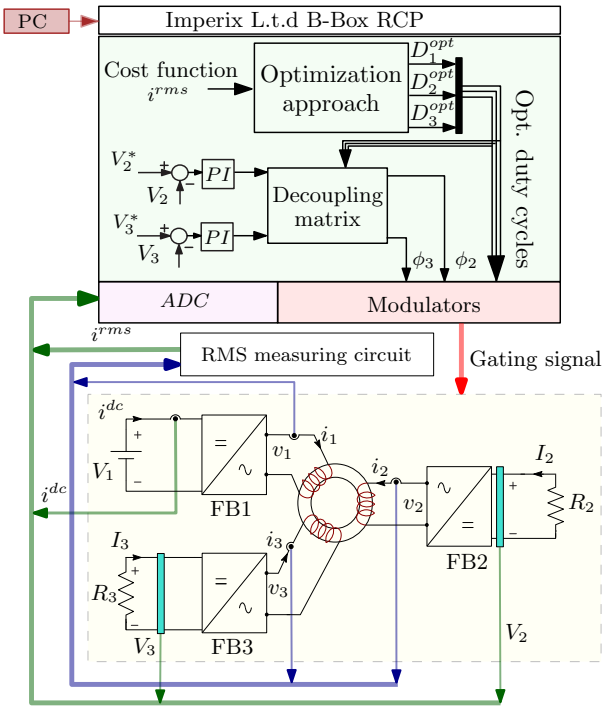

Fig. 11. Structure of the experimental setup.

B. Results of the Discussed Approaches

The results given by the three considered approaches and the simple PSM modulation are compared in this subsection and confronted with a BF characterization of the experimental prototype. A test case at low power with voltages mismatch at the three ports, with $V_1 = 400\text{V}, V_2 = 320\text{V}, V_3 = 480\text{V}, P_2 = 350\text{W}$, and $P_3 = 200\text{W}$, is considered in the following.

1) Offline Gradient Descent Optimization Results: Applying voltage and power conditions of the test case together with system parameters mentioned in Table. IV to the offline gradient descent algorithm described in Sec. II-A. The GDA generates the optimum duty cycles offline, at which the minimum total true rms current is obtained as illustrated in Fig. 12 The optimum duty cycles found by GDA are $D_1^{opt} = 0.23, D_2^{opt} = 0.25, D_3^{opt} = 0.155$, and the total true rms current $i^{rms} = 4.15\text{A}$. Fig. 13(a) shows voltage and current waveforms utilizing PSM, while Fig. 13(b) shows

TABLE IV
EXPERIMENTAL PROTOTYPE PARAMETERS

Parameters		Value
Nominal power at each port P_{rated}	kW	5
Switching frequency $f_S = 1/T_S$	kHz	40
Rated dc voltages $V_1 = V_2 = V_3$	V	400
Transf. turns ratio $n_1 : n_2 : n_3$		1:1:1
Transf. leakage inductances:		
Port-1 leakage inductance L_1	µH	40
Port-2 leakage inductance L_2	µH	47
Port-3 leakage inductance L_3	µH	41
Dead time	µs	1
Switching Devices		MMIX1Y100N120C3H1

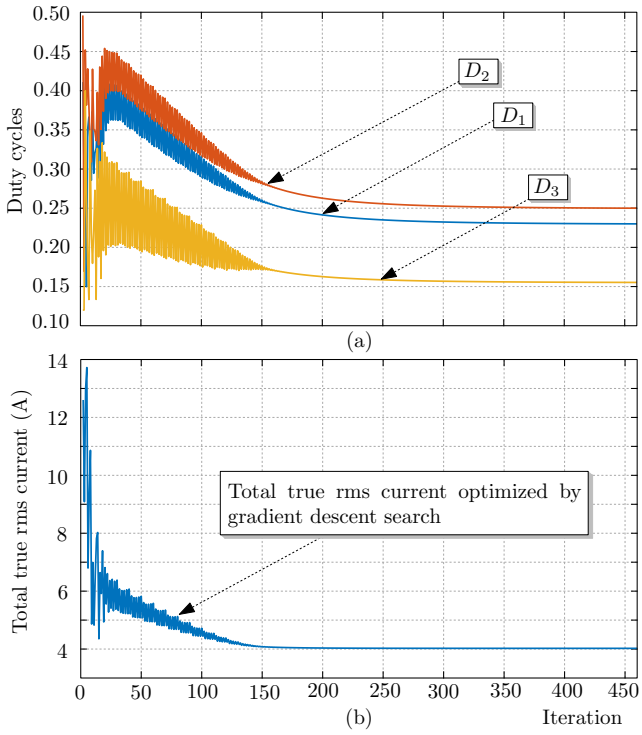

Fig. 12. Offline gradient descent optimization.

waveforms of the GDA optimization. The total true rms current reduced by about 60% of its original value compared to PSM.

2) Online Multidimensional Ripple Correlation Search Results: The same test case is optimized with 3D-RCC described in Sec. II-B. The search starts with the following initial duty cycles $D_1 = D_2 = D_3 = 0.4$ with total true rms current of about $i^{rms} = 10$A. The search runs online on the experimental prototype, as shown in Fig. 14. The found optimum point is at $D_1^{opt} = 0.21, D_2^{opt} = 0.23, D_3^{opt} = 0.145$ with $i^{rms} = 4.2$. The total rms current reduced by about 57% as compared to the initial value and by about 60% as compared to PSM. Fig. 13(c) shows the waveforms of the steady state search results with 3D-RCC.

3) Artificial Neural Network-Based Modulation Results: The ANN model has been implemented on the L.t.d B-Box RCP controller. The ANN model is run at a rate of 10 kHz, that is, 25% of the switching and control frequency. Measured voltages and powers of port-2 and port-3 are fed to the ANN as four inputs, while the ANN generates the optimum duty cycles based on the trained data. The result of optimizing the same test case is $D_1^{opt} = 0.205, D_2^{opt} = 0.218, D_3^{opt} = 0.1448$, at which $i^{rms} = 4.14$ A is obtained with a reduction of 60% as compared to PSM. Fig. 13(d) illustrates the waveforms of ANN-based modulation.

Fig. 15 compares the three approaches together with PSM and the BF results by means of experimental results, showing a slight deviation between the three approaches and the actual minimum found by BF search.

IV. Conclusion

This paper discusses and demonstrates three optimization approaches for achieving reduced rms operation of triple active bridge (TAB) converter. The discussed approaches are offline gradient descent algorithm (GDA), online multidimensional ripple correlation search (3D-RCC), and artificial neural network modulation based (ANN). Different characteristics emerged. GDA provides analytical analysis of a subset of the total possible switching patterns (favorable patterns) followed by a GDA search for optimum modulation variables, showing the possibility of having an accurate converter model for specific operating conditions. 3D-RCC provides an online model-free optimization technique that is effective regardless of the converter parameters. Finally, the ANN-based modulation provides a data-driven model of the TAB converter to overcome the problem complexity and allow prompt response times. The ANN is trained offline on optimum cases collected by PLECS simulation model.

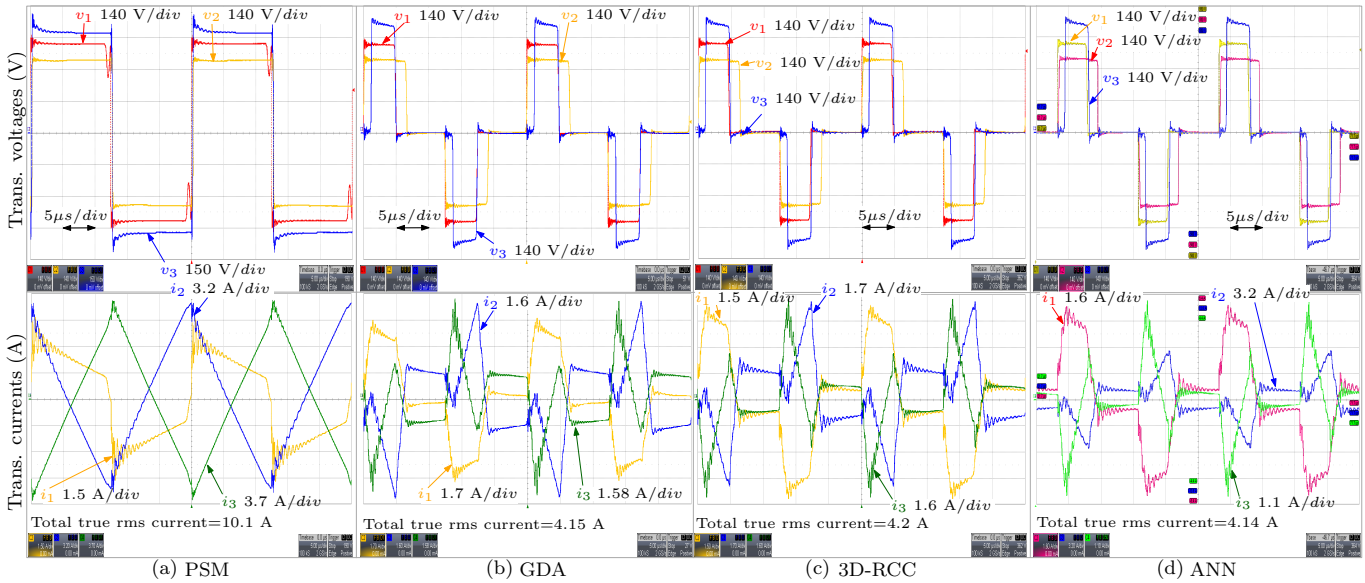

(a) PSM (b) GDA (c) 3D-RCC (d) ANN

Fig. 13. Transformer voltages and currents waveforms of the test case at which $V_1 = 400$V, $V_2 = 320$V, $V_3 = 480$V, $P_2 = 350$W, and $P_3 = 200$W.

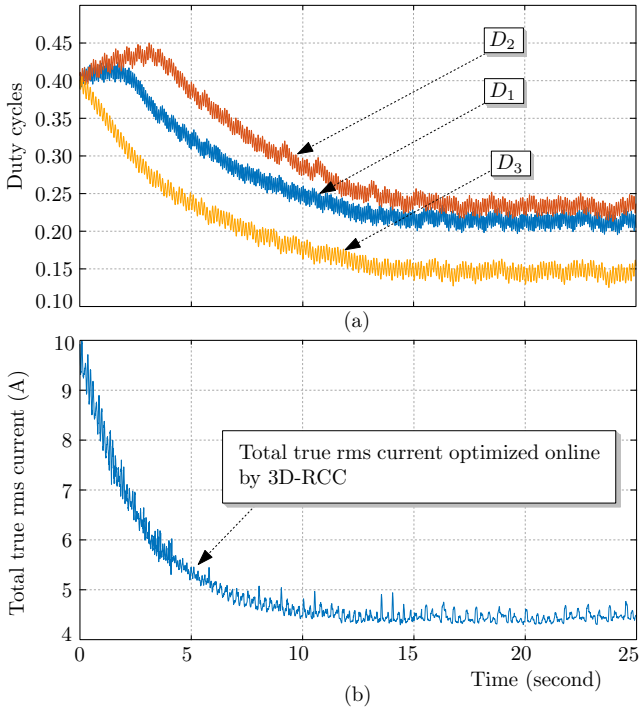

Fig. 14. 3D-RCC optimization.

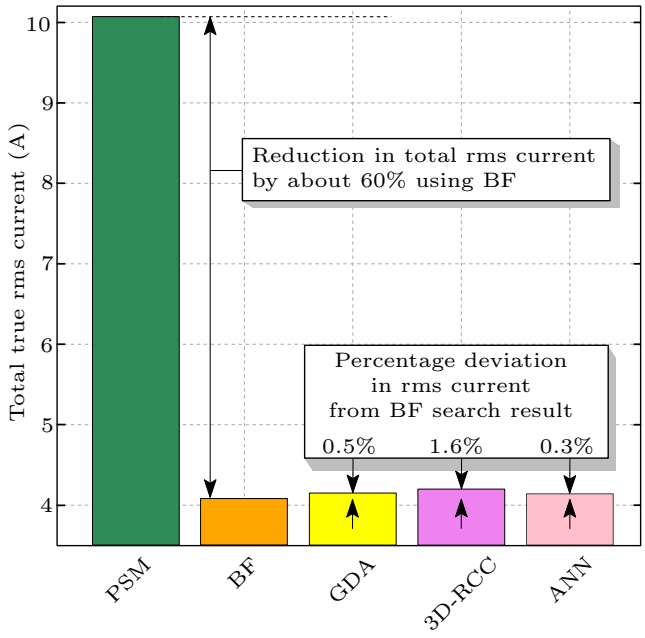

Fig. 15. Comparison of optimization approaches.

ACKNOWLEDGMENT

This work was supported in part by the Department of Management and Engineering (DTG), project "AIECO", University of Padova, and in part by the project MultiportGrid "Cross-Sectoral Energy Control through Interconnected Microgrids by Multiport Converter" funded within the call "ERA-Net Smart Energy Systems RegSys Joint Call 2018".

REFERENCES

[1] T. Pereira *et al.*, "A Comprehensive Assessment of Multiwinding Transformer-Based DC–DC Converters," *IEEE Trans. Power Electron.*, vol. 36, no. 9, pp. 10 020–10 036, 2021.

[2] M. Rashidi *et al.*, "Design and Development of a High-Frequency Multiport Solid-State Transformer With Decoupled Control Scheme," *IEEE Trans. Ind. Appl.*, vol. 55, no. 6, pp. 7515–7526, 2019.

[3] H. V M *et al.*, "An MVDC Based Meshed Hybrid Microgrid Enabled Using Smart Transformers," *IEEE Trans. Ind. Electron.*, pp. 1–1, 2021.

[4] M. A. Rahman *et al.*, "Design of a Multiloop Control Structure for Load-Disturbance Attenuation and Power-Mismatch Mitigation in Isolated Multiport Power Converters," *IEEE Trans. Ind. Electron.*, vol. 69, no. 9, pp. 8984–8996, 2022.

[5] A. Avila *et al.*, "A Modular Multifunction Power Converter Based on a Multiwinding Flyback Transformer for EV Application," *IEEE Trans. Transport. Electrific.*, vol. 8, no. 1, pp. 168–179, 2022.

[6] C. Gu *et al.*, "A Multiport Power Conversion System for the More Electric Aircraft," *IEEE Trans. Transport. Electrific.*, vol. 6, no. 4, pp. 1707–1720, 2020.

[7] C. Samende *et al.*, "Power Loss Minimization of Off-Grid Solar DC Nano-Grids—Part I: Centralized Control Algorithm," *IEEE Trans. Smart Grid*, vol. 12, no. 6, pp. 4715–4725, 2021.

[8] A. Vettuparambil *et al.*, "A Modular Multiport Converter to Integrate Multiple Solar Photo-Voltaic (PV) Modules With a Battery Storage System and a DC Microgrid," *IEEE Trans. Ind. Electron.*, vol. 69, no. 5, pp. 4869–4878, 2022.

[9] N. Naseem and H. Cha, "Triple-Active-Bridge Converter With Automatic Voltage Balancing for Bipolar DC Distribution," *IEEE Trans. Power Electron.*, vol. 37, no. 7, pp. 8640–8648, 2022.

[10] Y. Wu *et al.*, "A 150-kW 99% Efficient All-Silicon-Carbide Triple-Active-Bridge Converter for Solar-Plus-Storage Systems," *IEEE Trans. Emerg. Sel. Topics Power Electron.*, vol. 10, no. 4, pp. 3496–3510, 2022.

[11] C. Zhao *et al.*, "An Isolated Three-Port Bidirectional DC-DC Converter With Decoupled Power Flow Management," *IEEE Trans. Power Electron.*, vol. 23, no. 5, pp. 2443–2453, 2008.

[12] S. Dey and A. Mallik, "Multivariable-Modulation-Based Conduction Loss Minimization in a Triple-Active-Bridge Converter," *IEEE Trans. Power Electron.*, vol. 37, no. 6, pp. 6599–6612, 2022.

[13] P. Purgat *et al.*, "Zero Voltage Switching Criteria of Triple Active Bridge Converter," *IEEE Trans. Power Electron.*, vol. 36, no. 5, pp. 5425–5439, 2021.

[14] J. Li *et al.*, "Efficiency Optimization Scheme for Isolated Triple Active Bridge DC-DC Converter with Full Soft-Switching and Minimized RMS Current." *IEEE Trans. Power Electron.*, pp. 1–1, 2022.

[15] A. A. Ibrahim *et al.*, "Conduction Loss Reduction of Isolated Bidirectional DC-DC Triple Active Bridge," in *2021 IEEE Fourth International Conference on DC Microgrids (ICDCM)*, 2021, pp. 1–8.

[16] X. Wu *et al.*, "Model-Free Online Motion Adaptation for Energy-Efficient Flight of Multicopters," *IEEE Access*, vol. 10, pp. 65 507–65 519, 2022.

[17] A. A. Ibrahim *et al.*, "Artificial Neural Networks Approach for Reduced RMS Currents in Triple Active Bridge Converters," in *IECON 2022 48th Annual Conference of the IEEE Industrial Electronics Society*, 2022.

[18] J. W. Kimball and P. T. Krein, "Discrete-Time Ripple Correlation Control for Maximum Power Point Tracking," *IEEE Trans. Power Electron.*, vol. 23, no. 5, pp. 2353–2362, 2008.

[19] X. Li *et al.*, "Artificial-Intelligence-Based Triple Phase Shift Modulation for Dual Active Bridge Converter with Minimized Current Stress," *IEEE Trans. Emerg. Sel. Topics Power Electron.*, 2021.